



1 Skin Sea Surface Temperature schemes in coupled ocean- 2 atmosphere modeling: the impact of chlorophyll-interactive e-folding 3 depth.

4
5 Vincenzo de Toma², Daniele Ciani¹, Yassmin Hesham Essa^{1,3,4}, Chunxue Yang¹, Vincenzo Artale¹,
6 Andrea Pisano¹, Davide Cavaliere¹, Rosalia Santoleri¹, and Andrea Storto¹

7
8 ¹ CNR-ISMAR, Consiglio Nazionale delle Ricerche, Istituto di Scienze Marine, via
9 Fosso del Cavaliere 100, 00133 Rome, Italy.

10 ² CNR-ISMAR, Consiglio Nazionale delle Ricerche, Istituto di Scienze Marine, Calata Porta Di Massa - Porto Di Naples
11 80, 80133 Naples, Italy.

12 ³ GUF-IAU, Goethe University Frankfurt, Institut fuer Atmosphaere und Umwelt, Frankfurt, Germany

13 ⁴ ARC-CLAC, Agricultural Research Center, Central Laboratory for Agricultural Climate, Giza, Egypt

14

15 *Correspondence to:* Vincenzo de Toma (vincenzo.detoma@cnr.it)

16 **Abstract.** In this paper, we explore different prognostic methods to account for skin sea surface temperature
17 diurnal variations in a coupled ocean-atmosphere regional model of the Mediterranean Sea. Our aim is to
18 characterize the sensitivity of the considered methods with respect to the underlying assumption of how the
19 solar radiation shapes the warm layer of the ocean. All existing methods truncate solar transmission coefficient
20 at a constant warm layer reference depth; instead, we develop a new scheme where this latter is estimated from
21 a chlorophyll dataset as the e-folding depth of solar transmission. This allows spatial and temporal variations
22 of the warm layer extent to depend on seawater transparency. Comparison against satellite data shows that our
23 new scheme improves the diurnal signal especially during winter, spring, and autumn, with an averaged bias
24 on monthly scales year-round smaller than 0.1 K. In April, when most of the drifters' measurements are
25 available, the new scheme mitigates the bias during nighttime, keeping it positive but smaller than 0.12 K during
26 the rest of the monthly-averaged day. The new scheme implemented within the ocean model improves the old
27 one by about 0.1 K, particularly during June. All the methods considered here showed differences with respect
28 to objectively analyzed profiles confined between 0.5 K during winter and 1 K in summer for both the eastern
29 and the western Mediterranean regions, especially over the uppermost 60 m. Overall, the surface net total heat
30 flux shows that the use of a skin SST parametrization brings the budget about 1.5 W/m² closer to zero on an
31 annual basis, despite all simulations showing an annual net heat loss from the ocean to the atmosphere. Our
32 "chlorophyll-interactive" method proved to be an effective enhancement of existing methods, its strength
33 relying on an improved physical consistency with the solar extinction implemented in the ocean component.

34 1 Introduction

35 Air-sea fluxes govern the energy exchange at the ocean-atmosphere interface. A reliable representation of
36 the Sea Surface Temperature (SST) diurnal cycle, i.e. the typical SST oscillation/excursion between night and
37 day mainly due to solar heating, is crucial to accurately estimate air-sea heat fluxes (Kawai and Wada, 2007,
38 Soloviev and Lukas, 2013), whose direct measurement is very difficult. Indeed, diurnal warming events can
39 often exceed 5 K depending on weather conditions (Soloviev and Lukas, 1997) and geographical location,



40 typically at tropical and mid-latitudes but also occasionally at high latitudes (Karagali and Høyer, 2013). Large
41 diurnal warming events can lead to changes in air-sea heat flux locally reaching up to $60W/m^2$ (Fairall et al.,
42 1996, Ward, 2006, Kawai and Wada, 2007, Marullo et al., 2010, Marullo et al., 2016) on a variety of scales,
43 ranging from the short regional ocean weather ones to large seasonal or long-term ones.

44

45 Therefore, there is a wide interest in the development of models to accurately reconstruct SST diurnal variations
46 in order to improve the representation of air-sea energy exchanges, especially, but not solely, within the coupled
47 ocean-atmosphere modeling framework (Penny et al., 2019).

48 The net energy flux across the air-sea interface results from four contributions: the net solar radiation; latent
49 and sensible heat fluxes, and the net thermal radiation. The last three contributions depend on SST and have a
50 direct impact in determining ocean heat uptake or dynamical processes such as deep-water formation (Chen
51 and Houze Jr., 1997). Ideally, the most accurate flux estimate would imply the knowledge of the temperature
52 right at the atmosphere-ocean separation interface. From an observational point of view, the skin SST is the
53 temperature immediately adjacent to the ocean surface (~10-20 microns depth) that is measurable, typically
54 from infrared radiometers, and thus a key parameter to understand heat flux exchange (Minnet et al., 2019).
55 Indeed, following what is measurable by current sensors, the GHRSSST-PP (i.e. the Global ocean data
56 assimilation experiment High Resolution SST Pilot Project) introduced the distinction between skin, sub-skin,
57 depth, and foundation SST (Donlon et al., 2007), which can be respectively regarded as successive, better-to-
58 worse approximations to the ideal target, i.e. SST right at the interface, which is actually impossible to measure.
59 However, in most of the widely used ocean models and configurations, the too-coarse vertical resolution does
60 not allow to direct modeling skin SST (the first model layer being only around 0.5 - 1 meter thick, e. g. the
61 ocean model NEMO). Therefore, one must use schemes to reconstruct skin SST variations. Sadly, the only
62 thing one can be sure about is that in general no model will be able to perfectly reproduce skin SST diurnal
63 variations, and there are different ways to approach this challenging problem, each one still with its own
64 limitations (see Kawai and Wada, 2007 and references therein). Simplified models widely employed in ocean
65 and atmosphere state-of-the-art models parameterize the skin SST dynamics via the distinction of two main
66 effects: the cool skin and the warm layer. Due to its interactions with the atmosphere, the temperature right at
67 the ocean surface is supposed to be almost anywhere and anytime cooler than the ones below, resulting in the
68 ocean being covered with a cool skin layer: one of the very first and simpler models assumes this cool skin
69 temperature difference as proportional to the ratio between heat fluxes and kinematic stress (Saunders, 1967),
70 via the Saunders' constant.

71 The cool skin effect is very important in obtaining accurate estimates of the latent and sensible heat flux,
72 especially because its consideration modifies specific humidity at the ocean surface, which is one of the factors
73 in the bulk formula. Indeed, latent and sensible heat fluxes are defined as the heat transfer across the
74 ocean/atmosphere interface due to turbulent air motions (the former including the one resulting from
75 condensation or evaporation). For example, a recent study in the South China Sea showed that during nighttime
76 the cool skin temperature difference is around 1 K, and there's currently a large uncertainty in the Saunders'



77 constant (Zhang et al., 2020). A warm layer (in which diurnal warming effectively takes place) develops below
78 this cool skin, and its extent reaches a depth at which the penetration of solar radiation can be neglected (usually
79 fixed to 3m by most of existing parameterizations – see section 3.3 for more details). Diurnal warm layer
80 anomalies (which can sometimes exceed 3K) can potentially impact both the atmosphere and ocean mean state
81 on a variety of spatial (ranging from regional, basin-wide to global ones) and temporal scales (relevant for
82 weather or seasonal forecast to long-term climatic trends) (Donlon et al., 2007). The skin SST diurnal warming
83 amplitude increases under low surface winds (smaller than 2 m/s) and intense solar radiation (higher than
84 typical daily peaks, around 900 W/m²) conditions, smaller in winter and at the poles than in summer and in
85 the tropics. The accuracy of skin SST models, and therefore their ability to reconstruct skin SST diurnal
86 variations is crucial especially in heat budget closure problems, which are still a subject of active debate
87 especially in climate change hot spot regions such as the Mediterranean domain (see Marullo et al., 2021 and
88 references therein). Skin SST schemes are also crucial for assimilating daytime SST data from satellite sensors
89 (Penny et al., 2019; Storto and Oddo, 2019, Jansen et al., 2019), with obvious impact on the accuracy of
90 numerical weather and ocean predictions; a correct account of skin SST diurnal variations in turn is crucial for
91 flux calculations, which is already a very delicate problem also from an instrumental point of view.

92 Our main aim here is therefore to improve existing skin SST prognostic schemes, investigating the impact of
93 accounting for seawater's transparency conditions in modeling solar radiation extinction in the upper ocean.
94 The paper is structured as follows: after this introduction, we describe the data and coupled modeling system
95 in section 2. The mathematical context in which we developed our new method, whose novelty stands in
96 allowing the warm layer's extent to vary in space and time according to a chlorophyll-concentration climatology
97 follows in section 3. In section 4 we present results, discussing them and drawing conclusions in section 5.

98 **2 Data and Modeling System**

99 We describe here the data and the coupled regional modeling system used in this study. Our description here
100 is functional to the scope of this paper, and far from a complete depiction of each dataset. We redirect the
101 documentation and the appropriate literature describing each data and model in depth.

102 **2.1 Operational MED DOISST within CMEMS**

103 The MEDiterranean Diurnal Optimally Interpolated Sea Surface Temperature (MED DOISST) product,
104 operationally distributed and freely available within the Copernicus Marine Environmental Service (CMEMS)
105 provides gap-free (L4) hourly mean maps of sub-skin SST at 1/16° horizontal resolution over the Mediterranean
106 domain, covering from 2019 to present. Sub-skin SST is defined as the temperature at the base of the cool skin
107 layer, typically sensed by microwave radiometers, and representative of a depth of few millimeters from the
108 ocean's surface (Minnet et al., 2019).

109
110 This product combines satellite data acquired from the Spinning Enhanced Visible and InfraRed Imager
111 (SEVIRI) and model data from the Mediterranean Forecasting System (MedFS), respectively used as



112 observations and first guess for an optimal interpolation, giving a L4 field representative of subskin SST (see
113 Pisano et al., 2022 and references therein). In all diagnostics involving these data (and presented in the following
114 sections), regions where the percentage of model data is higher than 50% have been masked out both in
115 CMEMS MED DOISST and our experiments.

116 **2.2 iQuam in-situ data**

117 SST from drifter data were used for validation purposes and acquired from the iQuam (In situ SST Quality
118 Monitor) archive (Xu and Ignatov, 2014). The iQuam provides high-quality and quality controlled (QC) in-situ
119 SST data collected from various platforms, such as drifters, Argo Floats, ships, tropical and coastal moored
120 buoys. iQuam SST data are also provided along with quality level flags ranging from 0 to 5, with 5
121 corresponding to the highest quality level (Xu and Ignatov, 2014). For this study, SST with quality level equal
122 five were selected from drifters only, since they provide the temperature measurement closest to the surface
123 (compared to the other available instruments), ranging between 20-30cm (depending on the drifter type).

124

125 Additionally, we interpolated model outputs on drifters' location in time and space. Table S1 resumes the
126 number of available measurements for each given month and hour of the day. A total number of 555919 records
127 were available after the quality flag and platform selection, with the month of April being the most populated
128 one, with 222996 measurements, and 10361 measurements at 9:00 am.

129

130 **2.3 EN4 objective analysis**

131 EN4, the quality controlled subsurface ocean temperature and salinity profiles and objective analyses, were
132 used to assess the impact on the temperature vertical profiles. To facilitate the comparison, we made use of the
133 objective analyses after bias corrections of Expendable Bathythermograph (XBT) calibrations (Gouretski and
134 Reseghetti, 2010, Gouretski and Cheng, 2020), which give a gridded version of the dataset on a 1-degree regular
135 grid. In the comparison, model outputs were interpolated on this grid.

136 **2.4 Mediterranean Chlorophyll concentration**

137 Chlorophyll data were used to estimate e-folding depths' seasonality (see Methods, Section 3). These data
138 are a daily interpolation at 0.3 km horizontal resolution over the Mediterranean domain, and result from a
139 merging between multiple sensors (MERIS - MEdium Resolution Imaging Spectrometer from ESA, SeaWiFS
140 - Sea-viewing Wide Field-of-view Sensor and MODIS - Moderate Resolution Imaging Spectroradiometer from
141 NASA, VIIRS - Visible Infrared Imager Radiometer Suite from NOAA, and most recently the Copernicus
142 Sentinel 3A OLCI - Ocean and Land Colour Instrument), as detailed in the product description (see Volpe et
143 al., 2019 and references therein for further details).

144



145 2.5 ECMWF Atmospheric Reanalysis - ERA5

146 We used heat fluxes (net solar radiation, latent and sensible heat fluxes, net thermal radiation) from ERA5
147 at 0.25° horizontal and hourly temporal resolution (Hersbach et al., 2020) as reference for comparing
148 performances across simulations with different skin SST schemes. Despite their possible biases in air-sea fluxes,
149 atmospheric reanalyses at day are still widely thought to provide the best gap-free and dynamically consistent
150 reconstructions of the atmosphere system (Valdivieso et al., 2017, Storto et al., 2019).

151 2.6 Mixed Layer Depth 1969-2013 Climatology

152
153 Data from a mixed layer depth (MLD) climatology was used to test to what extent our modified scheme
154 correctly represents the seasonality of the mixed layer.
155 This monthly gridded climatology was produced using MBT, XBT, Profiling floats, Gliders, and ship-based
156 CTD (Conductivity, Temperature, Depth) data from different databases and carried out in the Mediterranean
157 Sea between 1969 and 2013. As for the model outputs, MLD is calculated with a $\Delta T = 0.1^{\circ}\text{C}$ criterion relative
158 to 10m reference level on individual profiles (Houpert et al., 2015a, Houpert et al., 2015b).

160 2.7 ISMAR Mediterranean Earth System Model (MESMAR)

161 MESMAR is a newly developed coupled regional modeling framework for the Mediterranean region (Storto
162 et al., 2023). MESMAR includes the following components:

- 163 • the ocean model: NEMO v4.0.7, with horizontal resolution of about 7 km, 72 vertical levels and a timestep
164 of 7.5 minutes (NEMO System Team, 2019);
- 165 • the atmosphere model: WRF v4.3.3, with 41 vertical hybrid levels and horizontal resolution of about 15
166 km, covering the European branch of the international Coordinated Downscaling Experiment (EURO-
167 CORDEX) domain, and a timestep of 1 minute (Skamarock et al., 2019);
- 168 • an interactive runoff model: HD v5.0.1, with a timestep of 30 minutes and 1/12° degree horizontal
169 resolution over Europe (Hagemann et al., 2020);
- 170 • the coupler: OASIS3-MCT, coupling the three models with a coupling frequency of 30 minutes, and
171 using the SCRIP library to interpolate fields between different model grids (Craig et al., 2017) ;

172 We report in figure 1 a graphical summary of different grids. Further details of its implementation, tuning, and
173 performances are described in (Storto et al., 2023).

174



175 3 Methods

176 Many schemes to reconstruct the skin SST diurnal variations rely on the existence of a cool skin and a warm
177 layer, respectively in the upper micrometers and few meters of the ocean, whose dynamics strongly depends on
178 wind conditions and solar radiation extinction within the upper ocean. To explain the rationale behind the
179 developments in our new method, we need to recap here some elements of this theory, which is mostly based
180 on Zeng and Beljaars, 2005 (named ZB05 hereafter) work.

181 We start from the one-dimensional heat transfer equation in the ocean:

$$182 \quad \frac{\partial T}{\partial t} = \frac{\partial}{\partial z} (K_w + k_w) \frac{\partial T}{\partial z} + \frac{1}{\rho_w c_w} \frac{\partial R}{\partial z} \quad (1)$$

183 in which the subscript w refers to water properties, T is seawater temperature, K_w is the turbulent diffusion
184 coefficient, k_w is the molecular thermal conductivity, ρ_w , c_w are respectively seawater density and heat capacity
185 per unit volume, R is the net solar radiation flux, defined as positive downward.

186 3.1 Cool Skin

187 We assume that there exists an oceanic molecular sublayer of depth δ , where K_w is negligible, and
188 temperature can be assumed constant in time, since it is always cooler than temperature of the underlying
189 seawater (Donlon et al., 2007, Zeng and Beljaars, 2005). Then integration of eqn. (1) gives, $\forall z \in [0, -\delta]$

$$190 \quad k_w \frac{\partial T}{\partial z} + \frac{1}{\rho_w c_w} [R(z) - R_s] - k_w \frac{\partial^2 T}{\partial z^2} \overset{\mathcal{O}(z^2)}{\nearrow} = const, \quad (2)$$

191 where R_s is solar radiation at the surface, assuming this constant to be the top boundary condition at $z = 0$:

$$192 \quad \rho_w c_w k_w \left. \frac{\partial T}{\partial z} \right|_{z=0} = Q = LH + SH + LW, \quad (3)$$

193 in which LH , SH , LW are respectively the surface fluxes of latent, sensible heat and net
194 long wave radiation.

195 Thus, eqn. (2) can be rewritten as

$$196 \quad \rho_w c_w k_w \frac{\partial T}{\partial z} = Q + R_s - R(z). \quad (4)$$

197 Making a further integration we get the cool skin temperature difference:

$$198 \quad T_s - T_{-\delta} = \frac{\delta}{\rho_w c_w k_w} (Q + f_s R_s), \quad (5)$$

199 where T_s and $T_{-\delta}$ are respectively the temperature at the upper (air-sea interface) and lower limits of the cool
200 skin layer, while f_s is the fraction of solar radiation absorbed in this layer:
201



202
$$f_s = \frac{1}{\delta} \int_{-\delta}^0 \left(1 - \frac{R(z)}{R_s}\right) dz,$$

203 which depends on the way radiation gets absorbed within the cool skin.

204 Eq. (5) is analogous to Saunders' model. Indeed, Saunders, 1967 was one of the first to construct a theory for
205 the ocean "cool skin" effect (already known from decades at those times), i.e. the observed temperature at the
206 air-sea interface is generally cooler than the temperature of the water at about 10 cm depth, especially during
207 nighttime. This effect takes place mainly because of the transfer of energy between the ocean and the
208 atmosphere, realized via heat loss and momentum transfers (wind stress). In a nutshell, at the end of its
209 derivation (Saunders, 1967), he obtains the following expression for the temperature difference across the cool
210 skin, ΔT_c :

211
$$\Delta T_c = \lambda \frac{Q v_w}{k_w (\tau / \rho_w)^{1/2}}, \quad (6)$$

212 where λ is the Saunders' proportionality constant, Q has already been defined above, τ / ρ_w is the kinematic stress
213 (ratio between wind stress module and seawater density), and v_w , k_w are respectively the kinematic viscosity and
214 thermal conductivity of seawater. Saunders' formulation was originally conceived for low, nonzero wind
215 conditions and neglecting the effect of solar radiation. As noticed by Artale et al., 2002 (named A02 hereafter),
216 with a constant λ , eqn. (6) becomes problematic in limiting cases of low and very high wind speeds (greater
217 than 7 m/s). Thus, they proposed to include a wind dependence in Saunders' constant, in order to still have a
218 finite, nonzero cool skin to bulk temperature difference even when the wind speed goes to zero or becomes very
219 high.

220 This scheme has proven to have good performances compared to other schemes also on a mooring site in the
221 Pacific Ocean (Tu and Tsuang, 2005).

222

223 3.2 Warm Layer

224 Below the skin layer, turbulent transfer is much more effective, and k_w can be neglected in favor of K_w .
225 Integrating eqn. (1) within the $[-d, -\delta]$ layer, we get:

226
$$\frac{\partial}{\partial t} \int_{-d}^{-\delta} T dz = \frac{Q + R_s - R(-d)}{\rho_w c_w} - K_w \frac{\partial T}{\partial z} \Big|_{z=-d}, \quad (7)$$

227 where d is a reference depth which can be assumed as the depth at which the diurnal
228 cycle can be omitted.

229 The turbulent diffusion coefficient can be expressed as (Large et al., 1994):

230
$$K_w = k u_{*w}(-z) / \phi_t \left(\frac{-z}{L} \right), \quad (8)$$



231 in which $k = 0.4$ is the Von Karman constant, z is negative in the ocean, u_{*w} is the friction velocity in the water
232 (this being the air friction velocity multiplied by the square root of air to sea density ratio), and the stability
233 function ϕ_t discriminates between a stable and an unstable regime, depending on the sign of its argument:
234 positive for the stable and negative for the unstable one. Assuming z to be negative in the ocean, the change of
235 sign entirely depends on the Monin Obukhov length, which is a length characterizing the prevalence of
236 buoyancy variations induced turbulence over the one generated by wind shear effects. This in turn is strongly
237 dependent on the sign of the net heat flux Q . If $Q > 0$, i.e. the ocean gains heat from the atmosphere, and we
238 have the stable regime: the diffusion coefficients decrease with increasing depth, favoring the downward heat
239 transfer within the water column. The opposite case, which favors transfer of heat from the ocean to the
240 atmosphere, can be modeled in different ways (see While et al., 2017 and references therein).

241 Assuming a temperature of dependence, for $d \gg \delta$ of the form

$$242 \quad T = T_{-\delta} - \left[\frac{z + \delta}{-d + \delta} \right]^\nu (T_{-\delta} - T_{-d}), \quad \nu \text{ empirical parameter} \quad (9)$$

243 eqn. (7) simplifies to

$$244 \quad \frac{\partial}{\partial t} (T_{-\delta} - T_{-d}) = \frac{Q + R_s - R(-d)}{d\rho_w c_w} \frac{\nu + 1}{\nu} - \frac{(\nu + 1)k u_{*w}}{d\phi_t(d/L)} (T_{-\delta} - T_{-d}) \quad (10)$$

245 In ZB05 scheme (Zeng and Beljaars, 2005), eqs. (5, 10) are the equations for the cool skin and warm layer
246 respectively. Assumptions on the fraction of solar radiation within this layer and the cool skin depth usually
247 follow Fairall et al., 1996 parameterization, whose detail are given in the Supplementary Material section.

248

249 3.3 Solar transmission expression

250 The expression of the solar transmission in Zeng and Beljaars, 2005 is

$$251 \quad \frac{R(-d)}{R_s} = \sum_{i=1}^3 a_i e^{-db_i}, \quad (a_1, a_2, a_3) = (0.28, 0.27, 0.45), \\ (b_1, b_2, b_3) = (71.5, 2.8, 0.07)m^{-1},$$

252 following Soloviev formulation (Soloviev, 1982) (S82 in the following), which is very widely used in
253 atmosphere models (such as WRF, Skamarock et al., 2019).

254

255 So far this is not the only possibility: a formulation with 61 coefficients has been developed by Jerlov, 1968,
256 which is based on different water types classified based on chlorophyll concentration and particulates, for light
257 in the visible spectrum.

258

259 A formulation with 9 coefficients (reported in Table 2) has been proposed to include such effects (Soloviev and
260 Schluskel, 1996, Gentemann et al., 2009) the first of them accounting for mean properties of I, IA, IB, II and
261 III Jerlov's optical water types. This formulation is widely employed in ocean models (such as in the optional



262 skin SST routine of NEMO, see While et al., 2017), with the reference depth d fixed to 3 m. So, the solar
263 transmission coefficient follows as:

$$264 \quad \frac{R(-d)}{R_s} = \sum_{i=1}^9 a_i e^{-db_i} \quad (13)$$

265 Ideally, one would like to have a reference depth representative of the one at which the transmission of solar
266 radiation is negligible, and if we take it as the depth at which transmission drops by $1/e$ from its surface value,
267 we get a value which can be different from $d = 3$ m, as we can see from figure 2a. Allowing for a realistic time
268 and space varying value of d represents the main novelty of our work.

269
270 From this viewpoint, choosing a value of $d = 3$ m while using the solar extinction formulation as in Soloviev,
271 1982 or Soloviev and Schluskel, 1996 would lead to underestimate the penetration of solar radiation into the
272 warm layer. Another possibility, as in the case of the NEMO module for radiation calculations (Jerlov, 1968,
273 Morel et al., 1989, Lengaigne et al., 2007), is to reconstruct a chlorophyll profile from its surface values and
274 employ an R-G-B scheme to calculate radiation as a function of depth. From eqn. (13) with only 4 terms (one
275 for chlorophyll, and three for R-G-B), one can numerically derive the e-folding depth using chlorophyll
276 variations and the R-G-B light extinction coefficients taken from lookup tables in the source code.

277
278 This would give a constant transmission throughout the basin, but with a spatially and temporally varying e-
279 folding depth and defines our new prognostic scheme for skin SST warm layer calculation. Everything else is
280 left unchanged, both the refinements of Takaya et al., 2010 (T10 hereafter) and the A02 model for cool skin.

281 3.3.1 E-folding depth estimates

282 Mediterranean Chlorophyll climatology data (see section 2.4) were re-gridded onto a 0.25° regular
283 longitude/latitude grid, and tabulated coefficients within NEMO were used to retrieve the transmission,
284 accounting for chlorophyll variations. E-folding depths then can be estimated as the depth at which transmission
285 drops by $1/e$ from its surface value. It can be noticed from figure 2b that also the e-folding depth varies with
286 seasonality, with typical values ranging from about 3 to 4.5 meters. This is the central point of our modification
287 to the prognostic scheme.

288 3.4 Overview of the simulations performed.

289 With the coupled ocean-atmosphere regional system we performed a set of four simulations, forced by
290 ERA5 in the atmosphere and ORAS5 (Zuo et al., 2018) in the ocean and covering three years (from 2019 to
291 2021), with hourly outputs (a synthesis is provided in Table 1):

- 292 1. a control run, in which no skin SST prognostic scheme is activated, therefore the diurnal SST variations
293 in the uppermost ocean layer (0.5 m thick) only come from the variability represented by the ocean model



294 at about 0.5 m of depth, considering also the 0.5 hours frequency of the coupling. We will refer to this
295 experiment in the following as *ctrlnoskin*;

296 2. a run in which the ZB05 scheme in WRF (Zeng and Beljaars, 2005) is active - we shall refer to this case
297 in the following as *wrfskin*;

298 3. a run in which the existing scheme within NEMO, which employ the 9-coefficient parameterization for
299 light extinction coefficients (Gentemann et al., 2009 - G09 hereafter), the scheme for the cool skin as
300 modified in A02, and refinements of the stability function, in the warm layer formulation as in T10 - we
301 shall refer to this as the *nemoskwrite* case;

302 4. a fourth simulation in which we modified the reference depth for the basis of the warm layer from $z = 3$
303 m , to an e-folding depth (i.e. the depth at which radiation gets diminished by $1/e$ from its surface value),
304 which is allowed to vary temporally and spatially because it is estimated from R-G-B light extinction
305 coefficients and chlorophyll concentration (see section 3) below. We will refer to it as *modradnemo*,
306 being the experiment where our modification to the skin SST scheme is implemented and tested.

307 The reason behind the choice of the above mentioned period of three years 2019-2021 is twofold: firstly, it
308 allows a validation against all the measurements from different data sources (satellite, drifters and objectively
309 analyzed profiles), and secondly, it is a good trade-off between the needs of keeping a reasonable computational
310 load, data volume for the analysis, and guarantees a minimal robustness of our finding, compared to a simulation
311 which covers just one year. However, we do not discard the possibility to extend the time coverage in our plans
312 for future works.

313 4 Results

314 In this section, we compare simulations outputs with data from different sources (see section 2), to assess
315 methods performances and impacts of our modifications. Since we are mainly acting to improve skin SST
316 diurnal variations reconstruction in the ocean component, the main focus is on the difference between the
317 *nemoskwrite* and *modradnemo*, while the *ctrlnoskin* and *wrfskin* ones are included as further reference elements
318 (the latter being not directly comparable because the atmospheric model sees the ocean foundation SST and
319 employ the scheme just to diagnose the skinSST).

320

321 4.1 Comparison with CMEMS MED DOISST

322 We calculated the mean diurnal warming amplitude in each season as the seasonally averaged diurnal
323 warming amplitudes (diurnal warming amplitude being defined for each day as the difference between daytime
324 maximum and nighttime minimum of SST), which can be cast into the following equation:

$$325 \quad (DWA)_{\text{seas}} = \frac{1}{N_{\text{seas}}} \sum_{i=0}^{N_{\text{seas}}} \left\{ \max_{h_i \in [10:00, 18:00]} - \min_{h_i \in [00:00, 06:00]} \right\} SST(h_i), \quad (14)$$



326 where seas = DJF, JJA, MAM, SON is the given season, N_{seas} is the number of days in that particular season
327 and h_i is the local time in hours for any given day.

328 Seasonally averaged diurnal warming amplitudes are shown in figure 3. On average, the maximum amplitude
329 is reached in summer, with the wrfskin simulation peaking at about 3 K, thus overestimating the mean diurnal
330 cycle compared to CMEMS MED DOISST (the monthly biases with respect to CMEMS foundation SST both
331 in the western and the eastern part of the Mediterranean Sea stay below 1 K year-round for every of the
332 simulations performed – see figure S1 in Supplementary Materials). The nemoskwrite simulation yields a
333 pattern very similar to CMEMS MED DOISST in summer, but underestimates the signal in the remaining
334 seasons. Outside the Summer season, our modifications yield a slight improvement (see modradnemo, last row
335 of figure 3). As expected, the control run in which no skin SST method is active, generally underestimates the
336 diurnal signal everywhere. Compared to nemoskwrite, the modradnemo simulation improves JJA mean diurnal
337 warming amplitude, especially over the Southern Mediterranean Sea, while in central and Northern part of the
338 basin tends to overestimate the signal by about 0.5 K with respect to CMEMS-DOI data. Furthermore, a general
339 underestimation is present also in DJF, with the modradnemo simulation showing the smallest differences with
340 respect to CMEMS-DOI data.

341 The spatial average over the whole Mediterranean domain is shown in figure 4, confirming the general
342 underestimation of the control run and the overestimation of the wrfskin (ZB05 scheme) in all seasons except
343 winter.

344 Spatially averaging highlights that our modification brings improvement, especially during wintertime, while
345 in all the other seasons the best agreement is gained by using the nemoskwrite setup (ZB05 with T10 and A02
346 modifications), at least according to the verification against CMEMS MED DOISST.

347 On a monthly timescale, figure 5 confirms that the control simulation tends generally to have a negative bias
348 of the diurnal amplitude, for the whole simulated period. The wrfskin (ZB05 scheme) shows a warm bias during
349 summertime months, shown just as a reference. The comparison between nemoskwrite (ZB05+A02+T10) and
350 modradnemo (chl e-folding depth) shows improvement of our scheme (modradnemo) over the old one
351 (nemoskwrite) especially in May, but not in June, despite in the rest of the period the amplitude of the bias is
352 slightly reduced.

353 4.2 Comparison with iQuam Star HR-Drifters

354 The bias with respect to drifter measurements averaged over drifters positions as a function of the month
355 and time of the day is shown in figure 6. All the schemes present a systematic cool bias in autumn (SON) for
356 most of the hours of the day. During April and June, the modradnemo simulation significantly reduced the
357 warm bias with respect to observations, compared to the nemoskwrite case, keeping it however generally



358 positive. This is quite reasonable, since drifters measurement can be thought representative of a depth which
359 can be also below the subskin level (typically of the order of some centimeters). Consistently with figure 5, the
360 wrfskin has a larger positive bias than modradnemo in June.

361

362 Further, as shown by figure 7, the bias between CMEMS MED DOISST and drifters is generally positive
363 anytime except in late spring/summer and autumn during nighttime. This pattern arises because of the
364 composite effect of having a temperature representative of the subskin level where and when there are data
365 from radiometers, and a temperature of about 1 *m* depth from the MEDFS system as first guess of the optimal
366 interpolation over cloudy regions (Pisano et al., 2022). However, the modified scheme significantly reduces the
367 difference, yielding a bias closer to the one of CMEMS MED DOISST with respect to drifters, especially during
368 April, which is the month in which the number of observations from drifters is definitely larger.

369 **4.3 Comparison with EN4 objective analysis**

370 Bias corrected vertical profiles gathered in an objective analysis were used to assess differences across
371 schemes along the water column. To summarize we report here only a macro subdivision into the eastern and
372 the western Mediterranean Sea, respectively in figures 8, 9. Model outputs were remapped on the same vertical
373 and horizontal grid. Looking at the mean profile averaged over all grid points in the given area, the agreement
374 is better for all simulations during summertime months, both for the eastern and the western region (see figs.
375 8c, 9c), showing in particular that the modradnemo simulation outperforms the nemoskwrite one. This is also
376 true for the wintertime season in the eastern Mediterranean (see fig.8b). On the other hand, in the western
377 Mediterranean all simulations tend to overestimate the signal, with our modified scheme doing a better job.
378 However, below about 80 *m* depth differences across schemes vanish.

379

380 Looking in more detail at the RMSE on the top 15 *m* depth between each simulation and EN4 as a function of
381 the month and more detailed region subdomains shown in figure 10a, we can see how in general all simulations
382 present the same pattern for the region outside of Gibraltar Strait, which can be thought an effect related to the
383 presence of the relaxation to horizontal boundary conditions, while for all the remaining regions and months
384 the control run, the wrfskin and the modradnemo present a similar pattern, with the modradnemo reducing the
385 RMSE in most of the regions and for most of the months, especially with respect to nemoskwrite, and this is
386 particularly true over the central Mediterranean Sea, in regions like Thyrrenian and Adriatic Seas.

387 **4.4 Heat fluxes and vertical propagation**

388 In this section we aim to characterize the differences of each scheme with respect to the control simulation.
389 We do this by specifically looking at the seasonality of Mixed Layer Depth (MLD), vertical profiles of
390 temperature in specific months and regions, and via the comparison of the net surface heat fluxes over the whole
391 Mediterranean Sea.

392



393 Compared to the Mixed Layer Depth climatology from 1969 to 2013 (Houpert et al., 2015a, Houpert et al.,
394 2015b, section 2.7), all of the tested schemes seems to have a similar impact on Mixed Layer Depth's
395 seasonality, with larger differences with respect climatological values being mostly located in the Eastern
396 Mediterranean Sea and during wintertime/spring (Figure 11). Figure 12 show how our modified scheme allows
397 more (less) vertical propagation of the diurnal signal during summer (winter) with respect to schemes with
398 constant e-folding depth in all central regions of the Mediterranean domain (regions 2, 3, 4 as defined in figure
399 10a), when all of them are referenced to the control simulation temperature daily minimum.

400 Indeed, from figure 12b, we can see that when all the temperature profiles for each simulation are referenced
401 to the ctrlnoskin daily minimum, there is a much wider diurnal warming signal for most of all the considered
402 depths level, with modradnemo representing an intermediate situation between the wrfskin and the nemoskwrite
403 simulation. This is probably due to the inclusion of chlorophyll-interactive variations, which allow for a better
404 representation of the variability of the mixed layer dynamics.

405 Estimates of the mean Mediterranean heat exchange between ocean and atmosphere based on previous studies
406 range from -11 to $+22$ W/m^2 , with an evident dominance of negative estimates, i.e., heat loss from the ocean to
407 the atmosphere (Jordà et al., 2017, Pettenuzzo et al., 2010). Some other studies suggest that the Mediterranean
408 heat budget is close to a neutral value, -1 W/m^2 (Ruiz et al., 2008) or $+1$ W/m^2 (Criado et al., 2012). Many
409 factors can contribute to such wide variability among different estimates, such as differences in the
410 parameterizations employed, initial and boundary conditions, and the way the physical processes, especially
411 through the Strait of Gibraltar are modeled (Macdonalds et al., 1994, Gonzales, 2023).

412

413 As shown by table 3, all simulations on an annual basis give a negative, non-closed balance for the net surface
414 heat flux, and modifications to include skinSST, performing very similarly one to another, bring the budget by
415 1.5 W/m^2 closer to zero, while ERA5 data show a positive net surface heat flux close to 5 W/m^2 . However, all
416 estimates fall into the (large uncertain) literature-based estimates. On seasonal timescales, the inclusion of
417 skinSST diurnal variations has the following effects:

- 418 • less net heat loss to the atmosphere during wintertime with respect to the control run (wrfskin differing
419 from the ctrlnoskin by about $6W/m^2$, while nemoskwrite and modradnemo having a similar impact, with
420 a difference of about $4W/m^2$ with respect to the control run);
- 421
- 422 • in springtime, all simulations show a positive imbalance, with the highest difference with respect to the
423 control run of about 1 W/m^2 in the modradnemo simulation;
- 424
- 425 • during summer, our modified scheme brings on average about 3 W/m^2 more than the control simulation
into the basin, yielding an estimate which is closer to ERA5;
- 426
- 427 • in autumn, our scheme cools down more than the control (about 2 W/m^2), being the farthest simulation
from ERA5 estimate, while traditional schemes tend to have a less negative net heat input.



428 All seasons except spring show larger difference with respect to ERA5 fluxes, with underestimation in summer,
429 and overestimation during winter and autumn, resulting in a bias of about 10 W/m^2 with respect to the net heat
430 flux annual budget in ERA5.

431 5 Summary and Conclusions

432 In this paper we studied the sensitivity of a regional coupled ocean-atmosphere-hydrological discharge
433 regional model on the Mediterranean Sea to prognostic schemes for skin sea surface temperature. Specifically,
434 we developed a new scheme which allows for spatial and temporal variations of the warm layer's extent
435 according to seawater's transparency conditions. This is possible by using tabulated solar extinction coefficients
436 already used in the ocean model, and inverting the functional form which determines how the solar radiation
437 varies along the vertical direction to find the depth at which this latter drops by $1/e$ from its surface value.

438

439 We simulated the period 2019-2021, analyzing hourly model outputs, and comparing aggregated results with
440 satellite, objectively analyzed and drifters data. Overall, the comparison with data shows that the new scheme
441 improves what is already implemented in NEMO, e.g. mean diurnal warming amplitudes are closer to satellite
442 observations in winter, spring and autumn, not being much worse than other existing schemes in summer, at
443 least looking at maps of mean diurnal warming amplitude grouped by seasons. Looking to the typical
444 temperature profile in both the eastern and the western Mediterranean Sea, non-negligible differences across
445 schemes stay confined in the topmost 20m (100m) of depth during summertime (wintertime). Regionally,
446 typical profiles are warmer than EN4 observation year-round for western regions (regions -1,1,2) especially in
447 winter, while regions in the east show a smaller RMSE in the topmost meters for basically all the regions and
448 months when comparing modradnemo to nemoskwrite. The Adriatic Sea has a systematically higher RMSE
449 with respect to EN4 in all the tested methods, for the whole period considered. In the central regions, the new
450 scheme penetrates temperature anomalies more (less) during summer (winter) months, having a less intense
451 mean diurnal warming amplitude signal in summer, especially over the upper few meters (the converse holds
452 for wintertime values). Therefore, with respect to the ctrlnoskin simulation, nemoskwrite shows the coldest
453 signal, the wrskin the hottest, and our modification modradnemo constitutes the middle situation, with milder
454 summer and winter than the control run. Therefore, future research efforts should be devoted to the better
455 characterization of this aspect, especially to understand if the modified vertical penetration of heat has some
456 particular effect on the dynamics of the mixed layer (see Song and Yu, 2017 and references therein). On a long-
457 term perspective, the method needs to be tested also in other areas and for longer periods, which can increase
458 the results' certainty and allow for usage in investigating impacts on relevant climate large-scale phenomena,
459 where the role of an improved diurnal warming signal could be more relevant (Bernie et al., 2007, Bernie et al.,
460 2008). These includes phenomena and physical processes such as propagation of Marine Heat Waves (MHW)
461 or deep water formation and deep convective events.

462

463



464 *Code and data availability*

465

466 The NEMO ocean model code (v4.0.7) is available at <https://forge.ipsl.jussieu.fr/nemo/wiki>.

467

468 The WRF atmospheric model code (v4.3.3) is available at <https://github.com/wrf-model/WRF>.

469

470 The HD hydrological discharge model (v5.1) is available at <https://zenodo.org/record/5707587#.Y-0VQ3bMKUk>.

471

472
473 The frozen version of the MESMARv1 code used in this manuscript is available at:
474 <https://doi.org/10.5281/zenodo.7898938>.

475

476 CMEMS MED DOISST Data downloaded from [CMEMS portal](#).

477

478 Chlorophyll data are freely available from [CMEMS portal](#).

479

480 The iQuam data version of this study used is V2.1, downloaded from the National Environmental Satellite,
481 Data, and Information Service Satellite Applications and Research [NOAA NESDIS STAR portal](#).

482

483 Gridded analyses of EN4 profiles are distributed from the [MetOffice Hadley Centre Observations](#) (we used
484 version 4.2.1).

485

486 ERA5 data are freely available after registration on the [Climate Data Store \(CDS\) by Copernicus Climate
487 Change Service \(C3S\)](#).

488

489 MLD data are distributed on a 0.25 degree regular grid, and freely available from the [Sea Open Scientific Data
490 Publication SEANOE portal](#).

491

492

493 Minimal data and scripts used within the manuscript to reproduce the figures in the manuscript are available at
494 this link:

495 <https://zenodo.org/records/10451206>

496



497 *Acknowledgments.* We specifically acknowledge Olivier Marti (LSCE/IPSL) and Aurore Voldoire (CNRM-
498 CNRS) for fruitful discussion during the 6th Workshop on Coupling Technologies for ESM held from 18 to 20
499 January 2023 in Toulouse, and Sophie Valcke (CERFACS) for their valuable support in the use of the NEMO
500 and WRF interfaces to the OASIS coupler. This Research is supported by ICSC – National Research Center for
501 High Performance Computing, Big Data and Quantum Computing, funded by Ministero dell'Istruzione,
502 dell'Università e della Ricerca through the NextGenerationEU programme.

503

504 *Author Contributions.* VdT and AS conceived the study and designed the experiments to conduct, VdT
505 Performed the simulation and data analysis, data downloading and writing of the first draft, VdT, DC, YH, CY,
506 VA, AP, DC, RS and AS equally contributed to discuss and interpret the results, finalizing the draft.

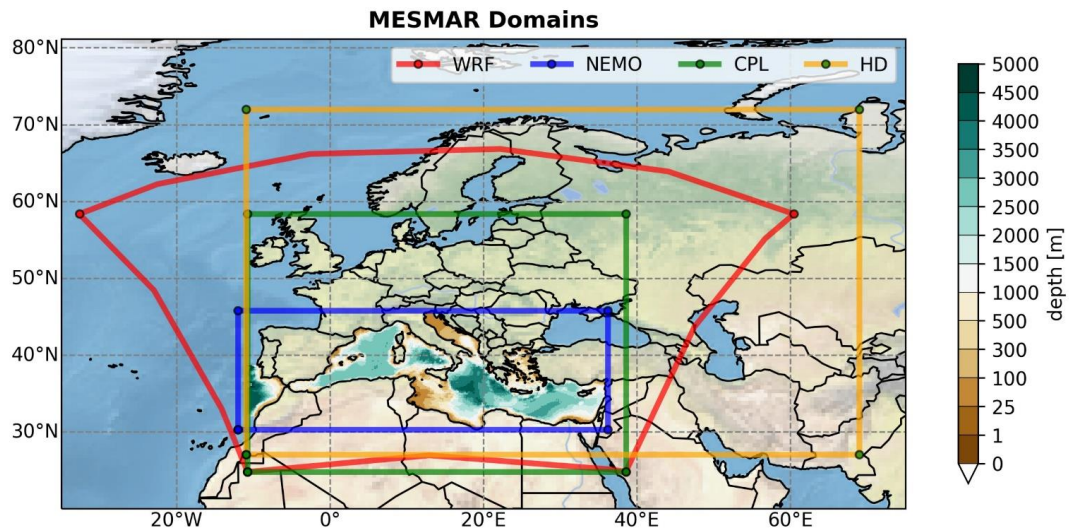
507

508 *Competing Interests.* All authors declare they have no competing interests.



509 **Figures**

510



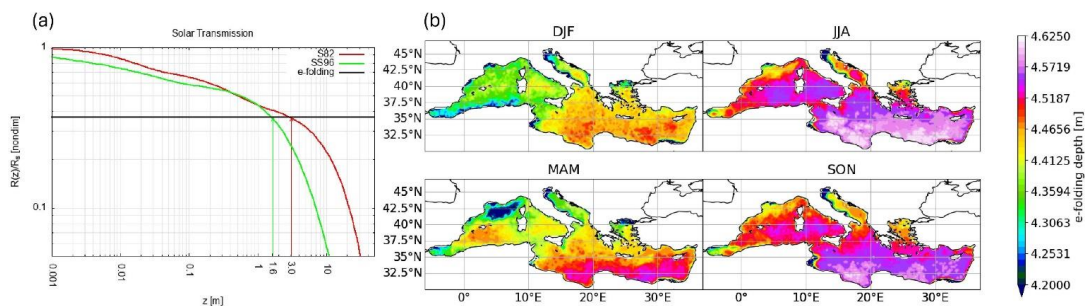
511

512 **Figure 1:** The modeling system domain: WRF, NEMO, HD and boundaries for the coupling mask are
513 respectively in red, blue, orange, and green. Contour filled plot shows the ocean model bathymetry.

514



515

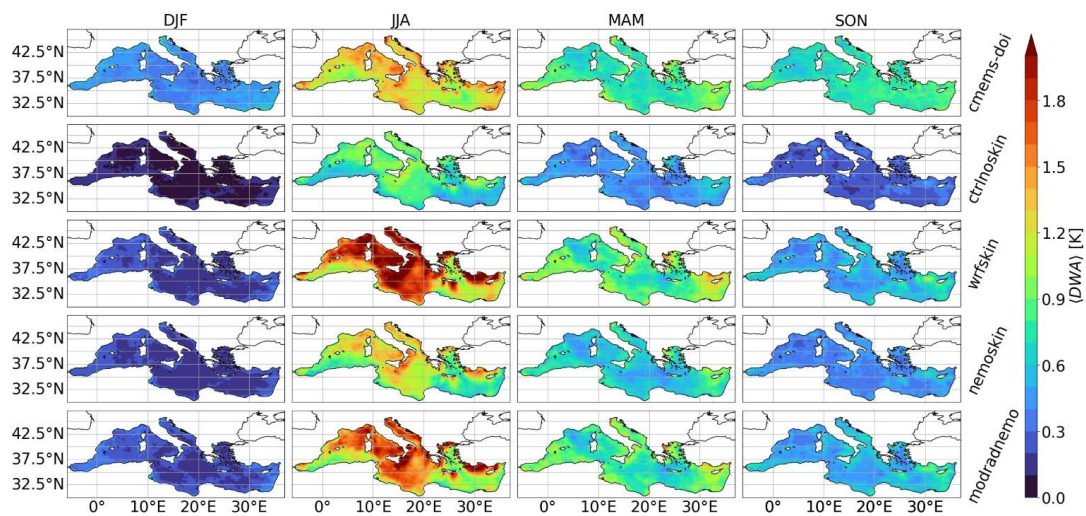


516

517 **Figure 2:** Panel 2a shows two different formulations frequently used for the transmission coefficient expression:
518 the red curve shows the formulation of Soloviev, 1982, while the green curve the one defined in Soloviev and
519 Schlüssel, 1996. Panel 2b shows e-folding depth estimates from Mediterranean Chlorophyll climatology of
520 Volpe et al., 2019: lowest values touch the 2.5 meters.



521
522



523

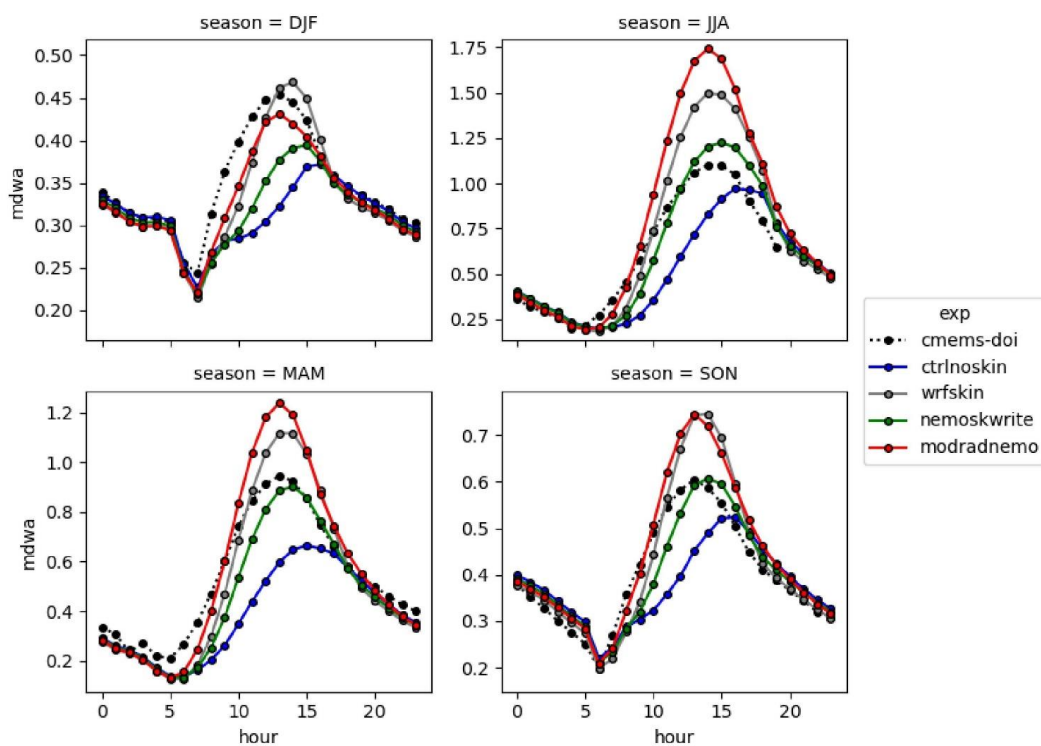
524 **Figure 3:** Mean diurnal warming amplitude averaged over seasons (on columns), for each case (row): the first
525 row is the CMEMS MED DOISST data, followed in order by the control simulation, wrf5skin, nemoswrite and
526 modradnemo.

527



528

529

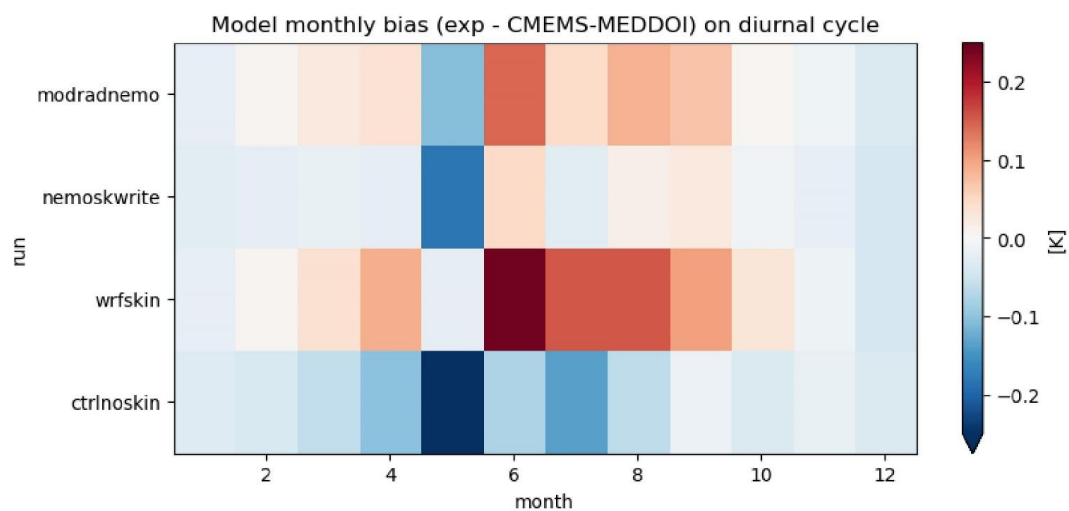


530

531 **Figure 4:** Seasonality of the diurnal cycle averaged over the whole Mediterranean Sea, masking out regions in
532 time and space where the percentage of model data in CMEMSDOI is greater than 50%.
533



534

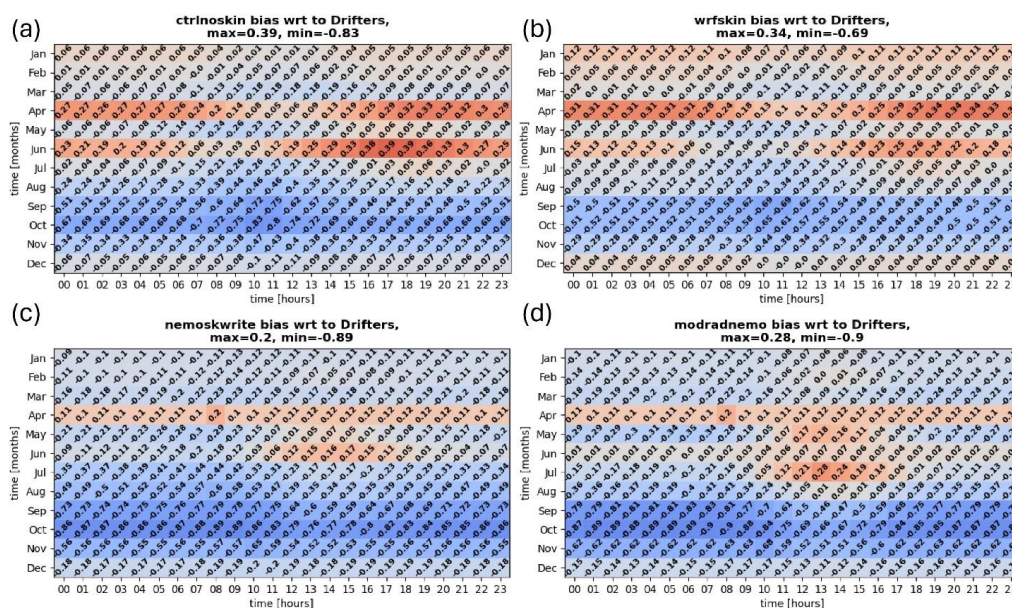


535

536 **Figure 5:** Monthly averaged values for the time series of spatial mean diurnal cycle over the Mediterranean Sea
537 (bias with respect to CMEMS MED DOISST)



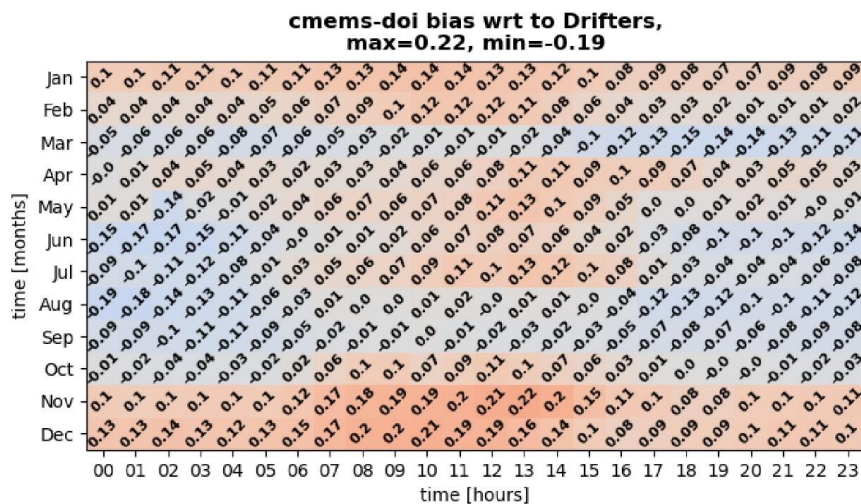
538



539
540 **Figure 6:** Bias with respect to measurements averaged over drifters' locations as a function of the month and
541 the time of the day. Panels 6a, 6b, 6c, 6d show respectively the results for all the simulations carried out in the
542 present study. Confidence on these numbers can be supported by the numbers of measurements reported in table
543 S1.
544
545



546

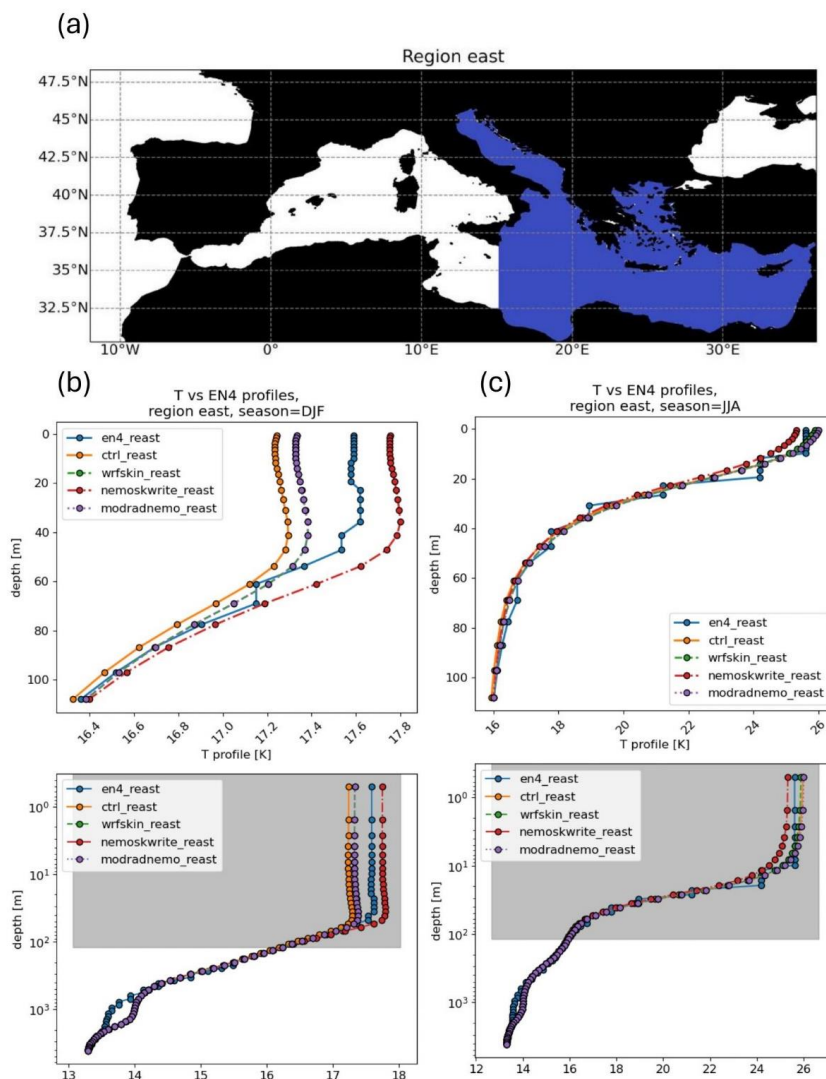


547

548 **Figure 7:** Bias with respect to measurements averaged over drifters' locations as a function of the month and
549 time of the day, for CMEMS MED DOISST data.
550



551



552

553

554

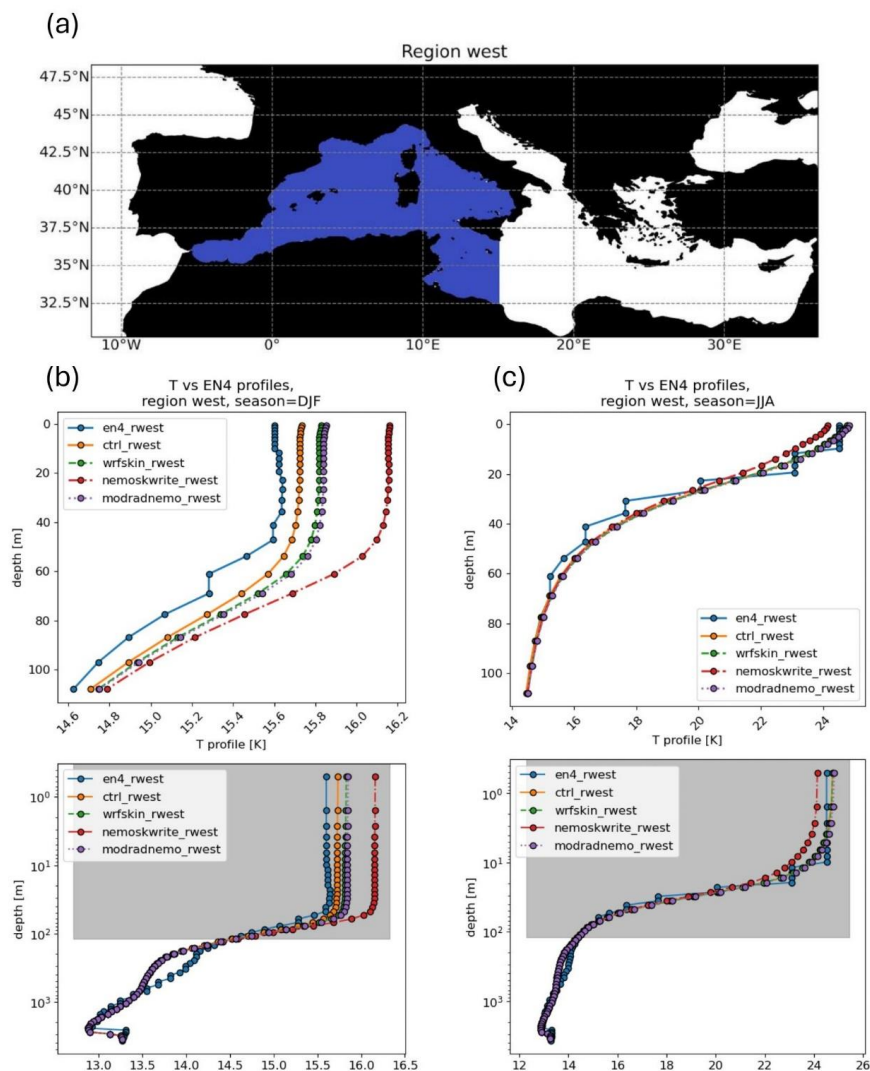
555

556

Figure 8: Spatial average of profiles within the eastern Mediterranean Sea, during winter and summer. Panel 8a shows the eastern region, while 8b, 8c show respectively wintertime and summertime spatially averaged profiles within the top 100 m in the upper part, on the bottom the whole depth range on a logarithmic scale.



557



558

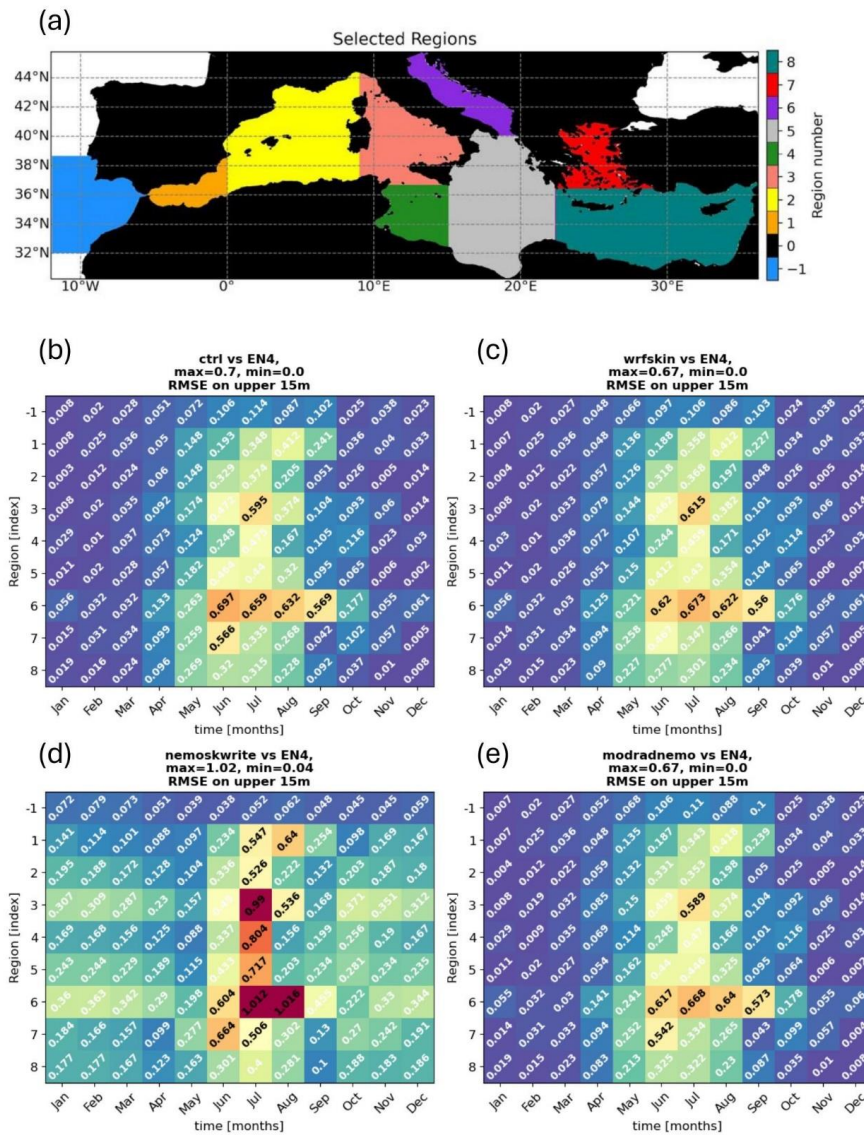
559

560

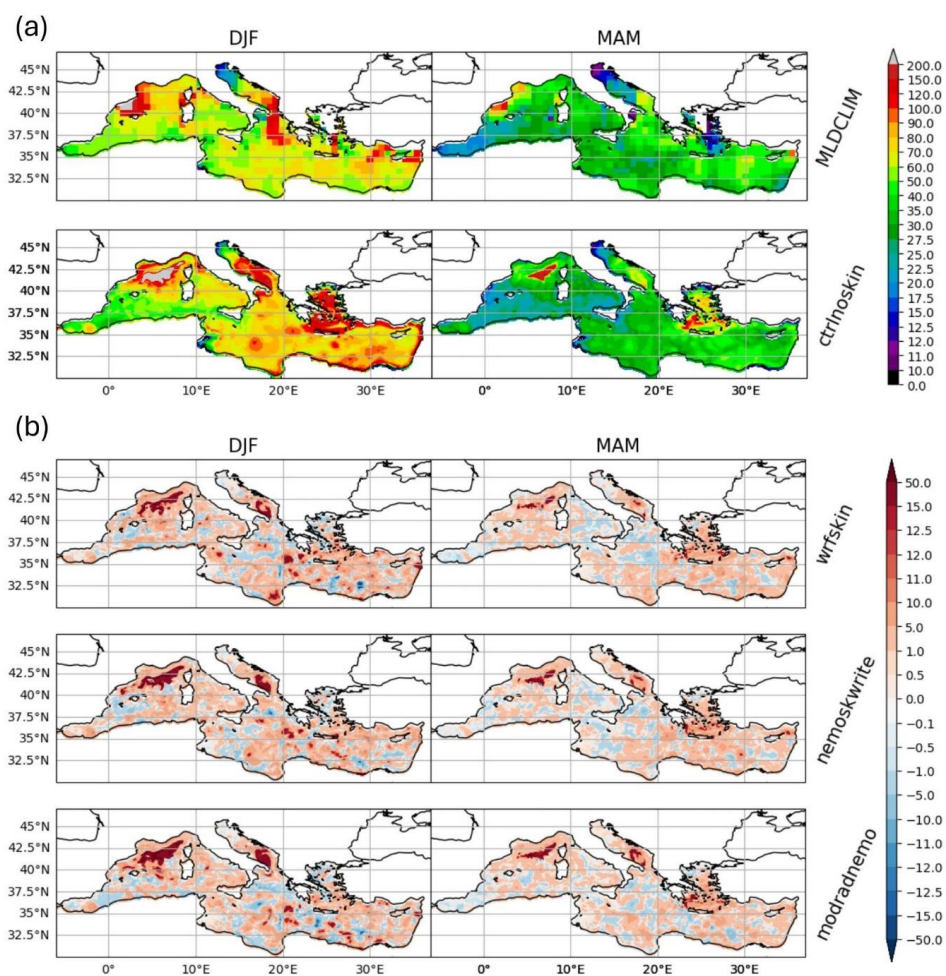
561

562

Figure 9: Spatial average of profiles within the eastern Mediterranean Sea, during winter and summer. Panel 9a shows the eastern region, while 9b, 9c show respectively wintertime and summertime spatially-averaged profiles within the top 100 m in the upper part, on the bottom the whole depth range on a logarithmic scale.



563
 564 **Figure 10:** RMSE on the top 15m of the difference between regionally averaged profiles between each
 565 simulation and EN4, displayed as a function of the region and the particular month. Division in regions is
 566 reported in panel 10a, while 10b, 10c, 10d, 10e show respectively the results for all the simulations carried out
 567 in the present study.
 568

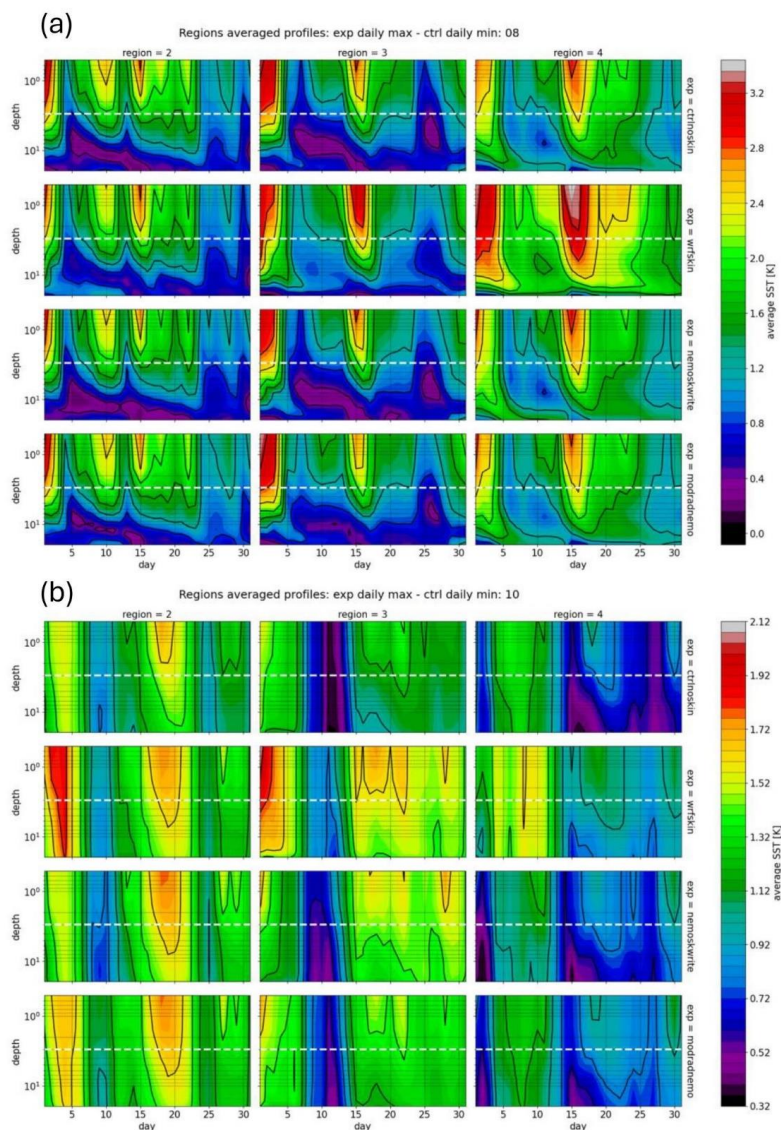


569
570
571
572
573
574
575
576
577
578
579
580
581
582
583
584
585
586
587
588

Figure 11: Maps of DJF, MAM of mixed layer depth for the climatology and for the control simulation in panel (a). Panel (b) shows the difference of the control with respect to each simulation. Units are meters.



589



590

591 **Figure 12:** Hovmoller plots for spatial average of model outputs temperature profiles in the regions 2,3,4 as
592 defined by figure 10a. Each row shows the difference between daily maxima for the given experiment minus
593 the daily minima for the control simulation. The white dashed line traces the $z = 3m$ line of the depth used as
594 reference for the base of the warm layer as in ZB05 scheme Zeng and Beljaars, 2005. Panel 12a shows August,
595 panel 12b shows October.
596



597
598 Tables
599

Simulation	Scheme active	Extinction coefficients in Warm Layer
ctrlnoskin	None	None
wrfskin	ZB05	SS82
nemoskwrite	ZB05+A02+T10	G09
modradnemo	ZB05+A02+T10	R-G-B + chl e-folding

600 **Table 1:** Overview of the simulations performed

601

Wavelength [μm]	i	a_i	b_i [m^{-1}]
0.3-0.6	1	0.2370	1.488×10^{-1}
0.6-0.9	2	0.3600	4.405×10^{-1}
0.9-1.2	3	0.1790	3.175×10^1
1.2-1.5	4	0.0870	1.825×10^2
1.5-1.8	5	0.0800	1.201×10^3
1.8-2.1	6	0.0246	7.937×10^3
2.1-2.4	7	0.0250	3.195×10^3
2.4-2.7	8	0.0070	1.279×10^4
2.7-3.0	9	0.0004	6.944×10^4

602 **Table 2:** Parameters for the Transmission coefficient following Soloviev and Schlu \ddot{u} ssel, 1996.



simulation	DJF	MAM	JJA	SON	Annual
ctrlnoskin	-173.31	133.92	75.56	-66.40	-7.55
wrfskin	-168.83	134.19	76.51	-65.87	-5.97
nemoskwrite	-169.28	133.79	76.77	-65.72	-6.10
modradnemo	-169.06	134.87	78.16	-68.13	-6.04
ERA5	-140.36	133.24	81.96	-53.46	5.35

603 **Table 3:** Averaged surface net heat flux over the Mediterranean Sea (W/m^2): seasonal and annual spatial
604 averaged mean values.

605



606

607

608 References

609

610 Artale, V., Iudicone, D., Santoleri, R., Rupolo, V., Marullo, S., and d’Ortenzio, F.: Role of surface fluxes in
611 ocean general circulation models using satellite Sea Surface Temperature: Validation of and sensitivity to the
612 forcing frequency of the Mediterranean thermohaline circulation. *Journal of Geophysical Research: Oceans*,
613 107(C8):29–1, 2002.

614 Bernie, D., Guilyardi, E., Madec, G., Slingo, J., and Woolnough, S.: Impact of resolving the diurnal cycle in an
615 ocean–atmosphere GCM. Part 1: A diurnally forced OGCM. *Climate Dynamics*, 29:575–590, 2007.

616 Bernie, D., Guilyardi, E., Madec, G., Slingo, J. M., Woolnough, S. J., and Cole, J.: Impact of resolving the
617 diurnal cycle in an ocean–atmosphere GCM. Part 2: A diurnally coupled C-GCM. *Climate dynamics*, 31:909–
618 925, 2008.

619 Chen, S. S. and Houze Jr, R. A.: Diurnal variation and life-cycle of deep convective systems over the tropical
620 pacific warm pool. *Quarterly Journal of the Royal Meteorological Society*, 123(538):357–388, 1997.

621 Craig, A., Valcke, S., and Coquart, L.: Development and performance of a new version of the OASIS coupler,
622 OASIS3-MCT 3.0. *Geoscientific Model Development*, 10(9):3297– 3308, 2017.

623 Criado-Aldeanueva, F., Soto-Navarro, F. J., & García-Lafuente, J.: Seasonal and interannual variability of
624 surface heat and freshwater fluxes in the Mediterranean Sea: Budgets and exchange through the Strait of
625 Gibraltar. *International Journal of Climatology*, 32(2), 286-302, 2012.

626 Donlon, C., Robinson, I., Casey, K., Vazquez-Cuervo, J., Armstrong, E., Arino, O., Gentemann, C., May, D.,
627 LeBorgne, P., Pioll’e, J., et al.: The global ocean data assimilation experiment high-resolution Sea Surface
628 Temperature pilot project. *Bulletin of the American Meteorological Society*, 88(8):1197–1214, 2007.

629 Fairall, C., Bradley, E. F., Godfrey, J., Wick, G., Edson, J. B., and Young, G.: Cool-skin and warm-layer effects
630 on Sea Surface Temperature. *Journal of Geophysical Research: Oceans*, 101(C1):1295–1308, 1996.

631 Gentemann, C. L., Minnett, P. J., and Ward, B.: Profiles of ocean surface heating (POSH): A new model of
632 upper ocean diurnal warming. *Journal of Geophysical Research: Oceans*, 114(C7), 2009.

633 Gonzalez, N. M.: Multi-scale modelling of Gibraltar Straits and its regulating role of the Mediterranean climate
634 (*Doctoral dissertation, Université Paul Sabatier-Toulouse III*), 2023.

635 Gouretski, V. and Cheng, L.: Correction for systematic errors in the global dataset of temperature profiles from
636 mechanical bathythermographs. *Journal of Atmospheric and Oceanic Technology*, 37(5):841–855, 2020.

637 Gouretski, V. and Reseghetti, F.: On depth and temperature biases in bathythermograph data: Development of
638 a new correction scheme based on analysis of a global ocean database. *Deep Sea Research Part I:
639 Oceanographic Research Papers*, 57(6):812– 833, 2010.

640 Hagemann, S., Stacke, T., & Ho-Hagemann, H. T.: High resolution discharge simulations over Europe and the
641 Baltic Sea catchment. *Frontiers in Earth Science*, 8, 12, 2020.

642 Hersbach, H., Bell, B., Berrisford, P., Hirahara, S., Hor’anyi, A., Mun’oz-Sabater, J., Nicolas, J., Peubey, C.,
643 Radu, R., Schepers, D., et al.: The ERA5 global reanalysis. *Quarterly Journal of the Royal Meteorological
644 Society*, 146(730):1999–2049, 2020.

645 Houpert L, Testor P, Durrieu de Madron X.: Gridded climatology of the Mixed Layer (Depth and Temperature),
646 the bottom of the Seasonal Thermocline (Depth and Temperature), and the upper-ocean Heat Storage Rate
647 for the Mediterrean Sea. SEANOE. https://doi.org/10.17882/46532_2015a.



- 648 Houpert, L., Testor, P., De Madron, X. D., Somot, S., D'ortenzio, F., Estournel, C., & Lavigne, H.: Seasonal
649 cycle of the mixed layer, the seasonal thermocline and the upper-ocean heat storage rate in the Mediterranean
650 Sea derived from observations. *Progress in Oceanography*, 132, 333-352, 2015b.
- 651 Jansen, E., Pimentel, S., Tse, W. H., Denaxa, D., Korres, G., Mirouze, I., & Storto, A.: Using canonical
652 correlation analysis to produce dynamically based and highly efficient statistical observation operators.
653 *Ocean Science*, 15(4), 1023-1032, 2019.
- 654 Jerlov, N. G.: *Optical Oceanography*. Amsterdam, London and New York: Elsevier Publishing Co, 1968.
- 655 Jordà, G., Von Schuckmann, K., Josey, S. A., Caniaux, G., García-Lafuente, J., Sammartino, S., ... & Macías,
656 D.: The Mediterranean Sea heat and mass budgets: Estimates, uncertainties and perspectives. *Progress in*
657 *Oceanography*, 156, 174-208, 2017.
- 658 Karagali, I. and Høyer, J.: Observations and modeling of the diurnal SST cycle in the North and Baltic seas.
659 *Journal of Geophysical Research: Oceans*, 118(9):4488–4503, 2013.
- 660 Kawai, Y. and Wada, A.: Diurnal Sea Surface Temperature variation and its impact on the atmosphere and
661 ocean: A review. *Journal of oceanography*, 63:721–744, 2007.
- 662
- 663 Large, W. G., McWilliams, J. C., and Doney, S. C.: Oceanic vertical mixing: A review and a model with a
664 nonlocal boundary layer parameterization. *Reviews of geophysics*, 32(4):363–403, 1994.
- 665 Lengaigne, M., Menkes, C., Aumont, O., Gorgues, T., Bopp, L., André, J. M., & Madec, G.: Influence of the
666 oceanic biology on the tropical Pacific climate in a coupled general circulation model. *Climate Dynamics*,
667 28, 503-516, 2007.
- 668 Macdonald, A. M., Candela, J., & Bryden, H. L.: An estimate of the net heat transport through the Strait of
669 Gibraltar. *Seasonal and Interannual Variability of the Western Mediterranean Sea*, 46, 13-32, 1994.
- 670 Marullo, S., Pitarch, J., Bellacicco, M., Sarra, A. G. d., Meloni, D., Monteleone, F., Sferlazzo, D., Artale, V.,
671 and Santoleri, R.: Air–sea interaction in the central Mediterranean Sea: Assessment of reanalysis and satellite
672 observations. *Remote Sensing*, 13(11):2188, 2021.
- 673 Marullo, S., Santoleri, R., Banzon, V., Evans, R. H., & Guarracino, M.: A diurnal-cycle resolving sea surface
674 temperature product for the tropical Atlantic. *Journal of Geophysical Research: Oceans*, 115(C5), 2010.
- 675 Marullo, S., Minnett, P. J., Santoleri, R., & Tonani, M.: The diurnal cycle of sea-surface temperature and
676 estimation of the heat budget of the Mediterranean Sea. *Journal of Geophysical Research: Oceans*, 121(11),
677 8351-8367, 2016.
- 678 Minnett, P., Alvera-Azcárate, A., Chin, T., Corlett, G., Gentemann, C., Karagali, I., Li, X., Marsouin, A.,
679 Marullo, S., Maturi, E., et al.: Half a century of satellite remote sensing of Sea Surface Temperature. *Remote*
680 *Sensing of Environment*, 233:111366, 2019.
- 681 Morel, A., & Berthon, J. F.: Surface pigments, algal biomass profiles, and potential production of the euphotic
682 layer: Relationships reinvestigated in view of remote-sensing applications. *Limnology and oceanography*,
683 34(8), 1545-1562, 1989.
- 684 NEMO System Team: *NEMO ocean engine*, 1288-1619 (isnn) edition, 2019.
- 685 Penny, S. G., Akella, S., Balmaseda, M. A., Browne, P., Carton, J. A., Chevallier, M., Counillon, F., Domingues,
686 C., Frolov, S., Heimbach, P., et al.: Observational needs for improving ocean and coupled reanalysis, S2S
687 prediction, and decadal prediction. *Frontiers in Marine Science*, 6:391, 2019.



- 688 Pettenuzzo, D., Large, W. G., & Pinardi, N.: On the corrections of ERA-40 surface flux products consistent
689 with the Mediterranean heat and water budgets and the connection between basin surface total heat flux and
690 NAO. *Journal of Geophysical Research: Oceans*, 115(C6), 2010.
- 691 Pisano, A., Ciani, D., Marullo, S., Santoleri, R., and Buongiorno Nardelli, B.: A new operational mediterranean
692 diurnal optimally interpolated SST product within the copernicus marine environment 2 monitoring service
693 3. *Earth System Science Data Discussions*, 2022:1–26, 2022.
- 694 Ruiz, S., Gomis, D., Sotillo, M. G., & Josey, S. A.: Characterization of surface heat fluxes in the Mediterranean
695 Sea from a 44-year high-resolution atmospheric data set. *Global and Planetary Change*, 63(2-3), 258-274,
696 2008.
- 697 Saunders, P. M.: The temperature at the ocean-air interface. *Journal of Atmospheric Sciences*, 24(3):269–273,
698 1967.
- 699 Skamarock, W. C., Klemp, J. B., Dudhia, J., Gill, D. O., Liu, Z., Berner, J., Wang, W., Powers, J. G., Duda, M.
700 G., Barker, D. M., et al.: A description of the advanced research WRF model version 4. *National Center for*
701 *Atmospheric Research: Boulder, CO, USA*, 145(145):550, 2019.
- 702 Soloviev, A.: On the vertical structure of the ocean thin surface layer at light wind. *Dokl. Acad. Sci. USSR,*
703 *Earth Sci. Serr*, pages 751–760, 1982.
- 704 Soloviev, A. and Lukas, R.: Observation of large diurnal warming events in the near-surface layer of the western
705 equatorial pacific warm pool. *Deep Sea Research Part I: Oceanographic Research Papers*, 44(6):1055–1076,
706 1997.
- 707 Soloviev, A. and Lukas, R.: The near-surface layer of the ocean: structure, dynamics and applications, *volume*
708 *48. Springer Science & Business Media*, 2013.
- 709 Soloviev, A. V. and Schlussek, P.: Evolution of cool skin and direct air-sea gas transfer coefficient during
710 daytime. *Boundary-Layer Meteorology*, 77(1):45–68, 1996.
- 711 Song, X. and Yu, L.: Air-sea heat flux climatologies in the Mediterranean Sea: Surface energy balance and its
712 consistency with ocean heat storage. *Journal of Geophysical Research: Oceans*, 122(5):4068–4087, 2017.
- 713 Storto, A., Alvera-Azcárate, A., Balmaseda, M. A., Barth, A., Chevallier, M., Counillon, F., ... & Zuo, H.: Ocean
714 reanalyses: recent advances and unsolved challenges. *Frontiers in Marine Science*, 6, 418, 2019.
- 715 Storto, A. and Oddo, P.: Optimal assimilation of daytime SST retrievals from SEVIRI in a regional ocean
716 prediction system. *Remote Sensing*, 11(23):2776, 2019.
717
- 718 Storto, A., Hesham Essa, Y., de Toma, V., Anav, A., Sannino, G., Santoleri, R., & Yang, C.: MESMAR v1: A
719 new regional coupled climate model for downscaling, predictability, and data assimilation studies in the
720 Mediterranean region. *Geoscientific Model Development Discussions*, 2023, 1-40, 2023.
721
- 722 Takaya, Y., Bidlot, J.-R., Beljaars, A. C., and Janssen, P. A.: Refinements to a prognostic scheme of skin Sea
723 Surface Temperature. *Journal of Geophysical Research: Oceans*, 115(C6), 2010.
- 724 Tu, C.-Y. and Tsuang, B.-J.: Cool-skin simulation by a one-column ocean model. *Geophysical research letters*,
725 32(22), 2005.
- 726 Valdivieso, M., Haines, K., Balmaseda, M., Chang, Y. S., Drevillon, M., Ferry, N., ... & Andrew Peterson, K.:
727 An assessment of air–sea heat fluxes from ocean and coupled reanalyses. *Climate Dynamics*, 49, 983-1008,
728 2017.



729 Volpe, G., Colella, S., Brando, V. E., Forneris, V., La Padula, F., Di Cicco, A., Sammartino, M., Bracaglia, M.,
730 Artuso, F., and Santoleri, R.: Mediterranean ocean colour level 3 operational / multi-sensor processing. *Ocean*
731 *Science*, 15(1):127–146, 2019.

732 Ward, B.: Near-surface ocean temperature. *Journal of Geophysical Research: Oceans*, 111(C2), 2006.

733 While, J., Mao, C., Martin, M., Roberts-Jones, J., Sykes, P., Good, S., and McLaren, A.: An operational analysis
734 system for the global diurnal cycle of Sea Surface Temperature: implementation and validation. *Quarterly*
735 *Journal of the Royal Meteorological Society*, 143(705):1787–1803, 2017.

736 Xu, F. and Ignatov, A.: In situ SST quality monitor (i-quam). *Journal of Atmospheric and Oceanic Technology*,
737 31(1):164–180, 2014.

738 Zeng, X. and Beljaars, A.: A prognostic scheme of sea surface skin temperature for modeling and data
739 assimilation. *Geophysical Research Letters*, 32(14), 2005.

740

741 Zhang, R., Zhou, F., Wang, X., Wang, D., & Gulev, S. K.: Cool skin effect and its impact on the computation
742 of the latent heat flux in the South China Sea. *Journal of Geophysical Research: Oceans*, 126(1),
743 2020JC016498, 2021.

744

745 Zuo, H., Balmaseda, M. A., Mogensen, K., & Tietsche, S.: OCEAN5: the ECMWF ocean reanalysis
746 system and its real-time analysis component (p. 44). Reading, UK: European Centre for Medium-
747 Range Weather Forecasts, 2018.